IEEE Access
Multidisciplinary | Rapid Review | Open Access Journal

Received February 4, 2021, accepted February 18, 2021, date of publication March 4, 2021, date of current version March 18, 2021.

Digital Object Identifier 10.1109/ACCESS.2021.3063736

Machine Learning-Based Corrosion-Like Defect Estimation With Shear-Horizontal Guided Waves Improved by Mode Separation

MATEUS GHEORGHE DE CASTRO RIBEIRO[1], ALAN CONCI KUBRUSLY[2], HELON VICENTE HULTMANN AYALA[1], AND STEVE DIXON[3]

[1]Department of Mechanical Engineering, Pontifical Catholic University of Rio de Janeiro, Rio de Janeiro 22451-900, Brazil
[2]Centre for Telecommunication Studies, Pontifical Catholic University of Rio de Janeiro, Rio de Janeiro 22451-900, Brazil
[3]Department of Physics, University of Warwick, Coventry CV4 7AL, U.K.

Corresponding author: Mateus Gheorghe de Castro Ribeiro (mateus-gheorghe@puc-rio.br)

This work was supported in part by the Coordenação de Aperfeiçoamento de Pessoal de Nível Superior (CAPES), Brazil, under Grant 001, in part by the National Council of Scientific and Technologic Development of Brazil (Conselho Nacional de Desenvolvimento Científico e Tecnológico—CNPq), and in part by the Carlos Chagas Filho Foundation for Research Support of Rio de Janeiro State (Fundação Carlos Chagas Filho de Amparo à Pesquisa do Estado do Rio de Janeiro—FAPERJ).

ABSTRACT Shear Horizontal (SH) guided waves have been extensively used to estimate and detect defects in structures like plates and pipes. Depending on the frequency and plate thickness, more than one guided-wave mode propagates, which renders signal interpretation complicated due to mode mixing and complex behavior of each individual mode interacting with defects. This paper investigates the use of machine learning models to analyse the two lowest order SH guided modes, for quantitative size estimation and detection of corrosion-like defects in aluminium plates. The main contribution of the present work is to show that mode separation through machine learning improves the effectiveness of predictive models. Numerical simulations have been performed to generate time series for creating the estimators, while experimental data have been used to validate them. We show that a full mode separation scheme decreased the error rate of the final model by 30% and 67% in defect size estimation and detection respectively.

INDEX TERMS Corrosion-like defect, mode conversion, neural networks, SH guided waves, structural health monitoring.

I. INTRODUCTION

Damage detection based on ultrasonic guided waves techniques has shown great potential for non-destructive testing (NDT) [1]–[9] and structural health monitoring (SHM) [10]–[17] applications. Among the different types of guided waves, shear horizontal (SH) guided waves are used widely, due to their characteristics such as simple dispersion relations and the displacement profiles of the modes. They are also unaffected by a non-viscous liquid in contact with the waveguide's surfaces, making them especially attractive for inspection of pipes [1], [5]. SH guided waves can be generated by Electromagnetic Acoustic Transducers (EMATs) [18], and can be used to detect defects from the scattered field produced when a guided wave mode is incident upon the defect [19]–[23].

The associate editor coordinating the review of this manuscript and approving it for publication was Shuping He.

Depending on the product of the SH mode's frequency and thickness of the plate or pipe, several SH guided wave modes can propagate. In such situations, when a single guided wave mode impinges upon a defect, the scattered field can be composed of several propagating modes, due to mode-conversion [20], [24]–[31]. The intensity of each mode that is present in the scattered field depends on the defect geometry. For corrosion-like defects, where thickness has been reduced to the extent that only the first two SH guided waves modes are able to propagate, it has been shown that the reflected and transmitted fields behave non-monotonically with defect geometry parameters, such as depth and the angle of the edge of the defect [20]. For higher-order modes, the non-monotonicity is even more accentuated [31]. This phenomenon complicates the interpretation of the received signal for defect sizing when operating at a frequency that supports several propagating modes. In addition to the non-trivial behavior of mode conversion, several modes may arrive at the

receiving transducer fairly close in time, producing a complex signal due to interference [32]. Although it is possible to detect the presence of the defect, which is useful for NDT screening systems [1], mode conversion and mode mixing make any accurate quantitative prediction of the defect size impractical without resorting to advanced signal extraction and interpretation techniques [20].

In this context, machine learning (ML) offers an advanced signal processing method that can be applied to provide defect size estimation, based on measurements related to guided waves phenomena [33]. As raw physical measurements can be hard to interpret [20], supervised learning paradigms can be effectively applied when enough labeled data is available. Predictive models based on ML [34] are able to provide better decision making, by decreasing false alarms and increasing computational performance [35].

Many papers deal with the problem of defect estimation using guided waves in different ways with ML, as described in a recent review [14]. Dib *et al.* addressed a problem of SHM using a network of piezoelectric sensors with ensemble learning by consensus, where individual learners with support vector machines use different sections of the time-series measurements. The features are based in Fourier transform coefficients, and experiments were carried out for estimating impact defect types under varying environmental conditions [36]. Simulated and experimental data have been used to train and test ML models respectively by García-Gomez *et al.* [37]. The authors used time and frequency domain feature engineering, feature selection with evolutionary algorithms, and artificial neural network models for detecting defects in pipes. This structure was also explored with a baseline extraction jointly with support vector machines [38].

Only recently, deep learning (DL) [39] was applied to SHM using guided waves. Its potential is great for this specific application, as it can automate the feature extraction process, and can also deal with high dimensional datasets. Melville *et al.* [40] employed convolutional neural networks to estimate the damage level of a thin metal plate, emulated by a steel washer, using full wavefield measured data. DL is also explored with Lamb waves, in which, wavelet coefficients are extracted and used as inputs of the models [41]. Moreover, Hesser *et al.* [42] have proposed an active source localization to predict the impact position of a steel ball in an aluminium plate, using numerical simulations to train and experimental data to validate ML models. Finally, Sun *et al.* [43] very recently proposed a damage classification in plates, using DL architectures jointly with SH guided waves. Three types of defects, namely, pinhole, crack, and flat-bottomed corrosion–like thinning, were examined in six different depths. In order to overcome the overlapping modes in the received signals, they adopted a variational mode decomposition to identify the signal components related to the modes, which facilitates time-of-flight determination and consequently, the position of the defect and plate thickness. However, the results were not very precise from a regression perspective; they explored simple architectures such as shallow or dense neural networks, which did not provide very good results, and also DL architectures, where the results were better.

A. CONTRIBUTIONS

In relation to recently published research into ML applied to damage evaluation with guided waves, the main contributions of this work are as follows:

1) Improvement of ML model results is obtained when applying a mode separation method to the guided waves signals, providing richer information on the defect. The procedure yields better estimation capability when applied to measured data. It is worth noting that a variational mode decomposition that is able to discriminate the signal component related to each mode has been used before [43], but that technique did not provide a precise extraction of the individual modes waveform, unlike the one adopted in this paper, and how the adopted mode decomposition acts as a facilitator in the ML pipeline was not assessed in previous work.
2) A damage estimation baseline-free data-driven model. The present method is baseline-free, in the sense that it does not depend upon pre-processing of all available data based on a comparison or subtraction of a nominal signal, which is a common procedure used in the literature [44]–[46].
3) Precise target variables for corrosion-like defect estimation. Specifically, we opted to generate continuous classification damage indices. In general, finer-grained damage indices such as the ones devised here are preferred, as they provide a greater amount of information for the decision-maker.
4) Adopting simulated signals in the construction of ML models and experimental signals for validation. This strategy is important since it avoids expensive measurement campaigns, and provides an effective means for creating datasets [37], [42].

In summary, this work is comprised of a method to detect and estimate corrosion-like defects in aluminium plates, based on using SH guided waves. The process is further improved by adopting a guided wave mode separation scheme, either in transmission or reception. The ML model was trained with simulated signals, obtained with a Finite Element Model (FEM), and then tested with experimental signals. The full mode separation scheme decreased the error rate of the final model. The overall data-driven modeling workflow is summarized in Fig. 1.

B. PAPER ORGANIZATION

The remainder of this paper is organized as follows. Section II reviews the basic concepts of SH guided waves, while in Section III the test bench is described, as well as the experimental procedure and measured data. The defect estimation method herein proposed and the results are given,

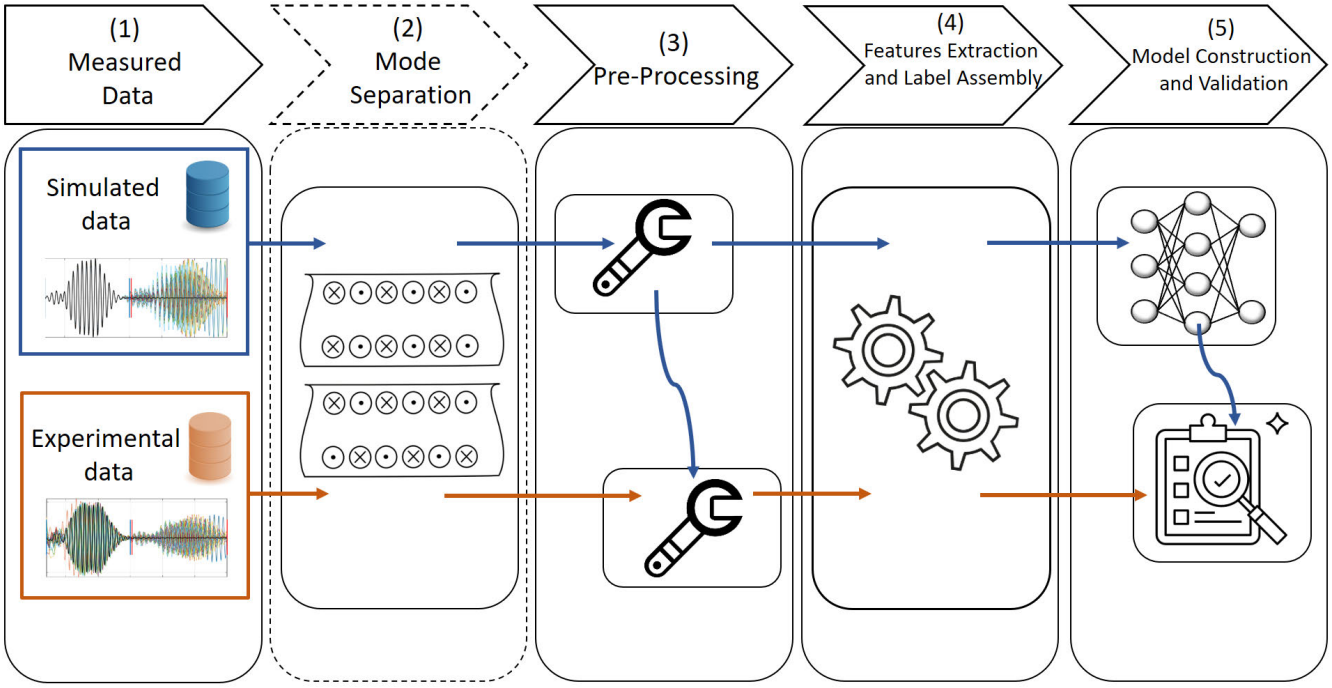

FIGURE 1. Overview of the modeling workflow solution adopted. Note that the simulated data is used in order to create the model, while the experiments are used to validate it. This workflow is general and may be replicated in other cases, where high fidelity computational models are available and a number of cases can be computed in a feasible time.

respectively, in Sections IV and V. The conclusions and suggested future work are highlighted in Section VI.

II. SH GUIDED WAVES IN PLATES

Shear horizontal guided waves in plates have in-plane polarized vibration, parallel to the surface of the plate, and perpendicular to the direction of propagation [47]. Adopting the coordinate system shown in Fig. 2, for an isotropic homogeneous plate, SH guided waves propagate along the x-direction and the displacement field is polarized in the z-direction.

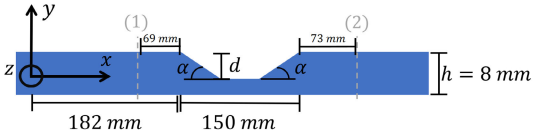

FIGURE 2. Plate and defect geometry. Generation is imposed at the origin and reception is either before and after the defect, in position (1) and (2) respectively. The corrosion severity is evaluated based on the relative area of the defect, which is dependent on d and α.

There are, potentially, infinite SH guided waves modes. Each mode has a different phase and group speed and mode displacement profile through the thickness of the sample, which is how the mode's displacement field varies along the y-coordinate within the plate, i.e $-h/2 \leq y \leq h/2$, where h is the thickness of the plate. The displacement profile is given by:

$$U_n(y) = \begin{cases} \cos(n\pi y/h), & n = \{0, 2, 4, \ldots\} \quad (1a) \\ \sin(n\pi y/h), & n = \{1, 3, 5, \ldots\} \quad (1b) \end{cases}$$

where n is the mode order. Note that in (1), even-order modes have a symmetric profile across the plate thickness, whereas odd-order modes are antisymmetric. On flat plates, the fundamental zero-order SH0 mode has a constant displacement along y and a phase and group speed equal to the medium's bulk shear (or transverse) wave speed, c_T for all frequencies, i.e. it is non-dispersive. All higher-order modes can propagate only for a frequency-thickness product above their respective cut-off values, given by

$$(fh)_{\text{cut-off}} = n\, c_T / 2 \quad , \qquad (2)$$

and their phase speed, c, depends on the frequency. The phase speed dispersion curves for the first three SH modes in an 8 mm thick aluminium plate are shown in Fig. 3.

If the operating frequency-thickness product is below the cut-off of the first-order mode, SH1, one operates in the low frequency-thickness regime, where only the SH0 mode can propagate. Otherwise, one operates in the high frequency-thickness regime [29], [30]. In the low frequency-thickness regime, when the SH0 mode impinges upon a corrosion-like defect, such as the thinning region shown in Fig. 2, part of it is reflected back and part of it is transmitted through the thinner region. On the other hand, in the high frequency-thickness regime, when any mode interacts with such a defect, there is mode conversion in either reflection or transmission [31]. This means that the received signal may be complex, due to the interference of several modes [32]. Additionally, in the high frequency-thickness regime, the transmission and reflection coefficients do

not behave monotonically [31], [48], as opposed to the low frequency-thickness regime [2]–[4], therefore rendering defect sizing difficult.

SH waves can be generated and received by periodic permanent magnet (PPM) electromagnetic acoustic transducers (EMAT) [49]–[51]. PPM EMATs impose a nominal wavelength, λ, on the generated SH waves. The frequency of the wave is imposed by the time-varying characteristics of the electric current pulse. Therefore, one can, in principle, select which mode is generated by matching its wavelength, or phase speed, at a specific frequency [50], since these parameters are related by $c = \lambda f$. Fig. 3 shows the line of 10 mm constant wavelength superposed on the SH dispersion curves. The frequency at which the dispersion curve of a mode of interest intersects the wavelength line, defines the optimum frequency to generate this specific mode. In the case illustrated in the Fig. 3, on this particular plate, the optimum operating frequency to generate the SH0 and SH1 modes are 311 kHz and 367 kHz, respectively.

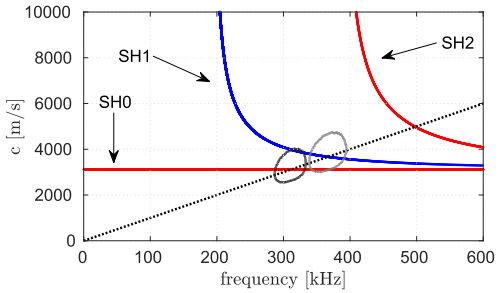

FIGURE 3. Phase speed dispersion curves for SH guided waves in an 8 mm thick aluminium plate. The dotted line corresponds to a 10 mm nominal wavelength. The continuous closed lines represent the -6 dB border of the operating region of 3 a cycle PPM EMAT, driven by an 8 cycle tone-burst at 311 kHz (black line) and 367 kHz (gray line).

However, due to the finite size of the PPM EMAT, there is a bandwidth of excitable wavelengths, instead of a single wavelength. The same holds for the frequency, since, usually, a tone-burst current is injected into the coil, which has a finite frequency bandwidth. This means that, even if the target frequency and wavelength to generate a specific mode are selected, other SH modes can be generated, if their dispersion curves cross the transducer operating region. The operating region is the locus defined by the intersection of both bandwidths [1], [20]. Fig. 3 shows the -6 dB border of the operating regions of a 3 cycle PPM EMAT, driven by an 8 cycle tone-burst at 311 kHz and 367 kHz. As can be seen, in this case, when attempting to generate the SH0 mode, the SH1 mode is also generated with non-negligible intensity, since it lies within the operating region of the SH0 mode. The same holds true for generating the SH1 mode. Mode selectivity can be enhanced by using some kind of mode separation [52]–[55].

III. CASE STUDY

In this paper, signals due to the interaction of SH guided waves in an aluminium plate with wall thinning defects were used to extract features for a ML model, used to estimate the corrosion-like defect severity. The setup follows [20], [48]. The geometry of the plate can be observed in Fig. 2. The plate is 8 mm thick with a 150 mm long thinning region starting at 182 mm from the origin, where transmission occurs. Either its depth (d) and edge angle (α) were varied. Reception is performed either before the defect or after it, at positions (1) or (2) in Fig. 2, respectively.

Numerical data were obtained by means of a commercial, time-domain, Finite Element Method (FEM) solver, OnScale Solve^{TM} (former PZFlex©), which allows simulation of SH waves in a two-dimensional model. SH waves in the FEM model were excited, mimicking the spatial force distribution produced by a PPM EMAT. This was performed by imposing a spatial force distribution with a 10 mm period and the same number of cycles as the EMAT to the surface of the model in the direction of the polarization of the SH waves, i.e., perpendicular to the propagation direction parallel to the plates' surface. Forces are then modulated by the same time history as the exciting current applied to the EMATs in experiments. This approach allows the generation of SH guided waves, without the need for including the EMAT in the model, as validated previously [1], [20], [31], [32], [51], where the high-representability of the simulated and experimental signals were verified. The excitation forces were applied either in the top or bottom surfaces, in order to provide enough signals for the mode separation procedure. The material density was set to $2698\,kg/m^3$, and the transverse wave speed equal to $3111\,m/s$. A mesh with 50 elements per wavelength was used. Due to the variation of α and d (see Fig. 2), the dataset created has approximately 1230 defect cases, which were generated in an almost automatic fashion, while in the experiment any new sample requires complicated machining for specimen thinning.

Experimental data were acquired using a RITEC ©RPR-4000 Pulser/Receiver, connected to PPM EMATs with 10 mm nominal wavelength from Sonemat Ltd, used as transmitter and receiver. The signal from the receiver EMAT is amplified and then acquired with an oscilloscope linked to a computer. The test samples were 800 mm long and 250 mm wide plates. The experiment was carried with 34 samples, one instance is the nominal condition (without defect) and the other 33 samples with variations of α (10°, 45°, and 90°) and d (1 mm, 2 mm, 3 mm,..., 7 mm), with $\alpha = 55°$ varying d (2 mm, 3 mm,..., 7 mm), plus six additional samples, namely, $d = 6$ mm at $\alpha = 25°$, 30° and 35° and $d = 7$ mm at $\alpha = 25°$, 30° and 65°. These sample geometries were also used in previous work for comparison [20], [48]. The excitation pulse was set to an 8 cycle tone burst at either 311 kHz or 367 kHz, in order to predominantly generate the SH0 or SH1 modes, at a 10 mm nominal wavelength, respectively. Both modes can be generated and received in this case. Thus, in this paper, we assess whether mode separation further improves the ML model accuracy.

In order to separate the SH0 and SH1 modes, we adopted dual transduction in either transmission or

reflection [56], [57]. Dual excitation consists of positioning transmitter transducers on both the upper and lower surfaces of the plate at the same longitudinal position. If the forces imposed by both transducers are in-phase, resp. out-of-phase, then only symmetric, resp. anti-symmetric modes are generated. As explained in [56], both arrangements of these forces can be obtained by connecting two EMATs in series, in direct or reverse polarity. Alternatively, one can add or subtract the response signal as follows:

$$u_S = (u_T + u_B)/2 \quad , \tag{3a}$$
$$u_A = (u_T - u_B)/2 \quad , \tag{3b}$$

where u is the signal of interest, the subscripts S and A are for the symmetric and antisymmetric parts respectively, and the subscripts T and B stand for generation taking place at the top or bottom surfaces, respectively. Equation (3) also holds for reception: by properly combining the signals from receivers in both surfaces, symmetric or antisymmetric modes are separated in the received time-domain.

This procedure can be applied to the transmission step alone, here called *mode-separation in transmission*, where a pure mode, whether SH0 or SH1, is generated at its respective optimum frequency. It can also be applied in both the transmission and reception of the signals, namely *fully mode-separation*. Therefore a pure mode is generated, and mode mixing originated in reflection or transmission through the defect is extinguished. Additionally, no mode separation was also adopted as a reference. This case consists of the most common situation, where there are just one transmitter and one receiver, positioned on one of the surfaces of the plate. It is referred to here as the raw signals or *non-separated* case.

The mode-separation technique described here requires access both surfaces of the plate, with the correct alignment between the position of the upper and lower transducers. A detailed assessment of the technique is presented in [56]. Other strategies for mode separation and selectivity do exist such as [43], [52]–[55] that may impose less restrictive measurement conditions, but, on the other hand, may require additional processing or a more complicated excitation procedure. The main goal here is to assess whether being able to distinguish the signals, and the corresponding features, associated with the possible propagating modes in the high-frequency-thickness regime, leads to improved performance of the defect sizing estimation procedure.

The *fully mode-separated* signals for a purely generated SH1 mode are shown in Fig. 4, for numerically simulated signals. The thicker black line indicates the non-defective plate, and the different grey-scale lines indicate signals obtained for different defect severities, where a lighter color corresponds to a more severe defect (greater relative area), and a darker color corresponds to a less severe defect; the color-severity relation is described by the color bar. Fig. 4(a) shows the SH1 reception before the defect, position (1), at around 50 μs one can see the direct pulse is the same for all cases, since this first pulse does not interact with the defect. At around 90 μs,

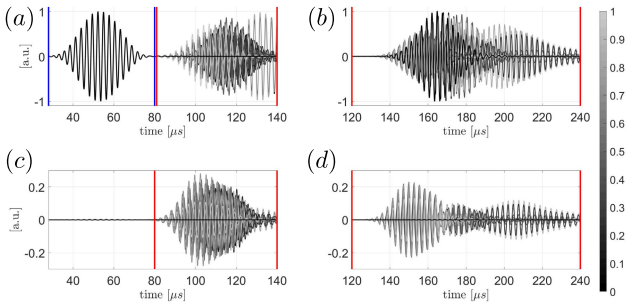

FIGURE 4. Simulated *fully mode-separation* signals for purely SH1 generated at 367 kHz. Reception of the separated SH1 mode (a) and (b) and separated SH0 mode (c) and (d). Reception before the defect, at position (1), (a) and (c) and after the defect, position (2), (b) and (d). The severity of the defects is given by the color bar.

the reflected SH1 is observable, which is different for the several defect cases, due to the interaction of different defect geometries. The amplitude of the reflected signals varies considerably, depending on the defect geometry; in some cases reaching amplitudes almost as high as the incident signal, due to the phenomenon of total reflection [20], [27], [28], for very low edge angle thinning, even for defects that are not very deep, and thus presenting moderate severity. Fig. 4(b) shows the SH1 after the defect, position (2), showing differences for several geometries used. Fig. 4(c) and (d) show the separated SH0 in reception due to the pure SH1 transmission, for positions (1) and (2), respectively. As can be seen, there is no direct pulse around 50 μs in position (1), since the SH0 mode is not generated. Similarly, reflected and transmitted signals differ for each defect geometry.

Similar signals were obtained for the experimental setup. These are shown in Fig. 5. One can see that, in this case, the direct pulse, around 50 μs in Fig. 5(a), has slight phase differences, due to the experimental positioning error among experiments. There is some non-zero signal at this time interval for the SH0 separated in reception, shown in Fig. 5(c). The latter also shows features due to positioning errors, which more severely affects selecting the mode with opposite polarization, as explained in [56]. One can also observe that for

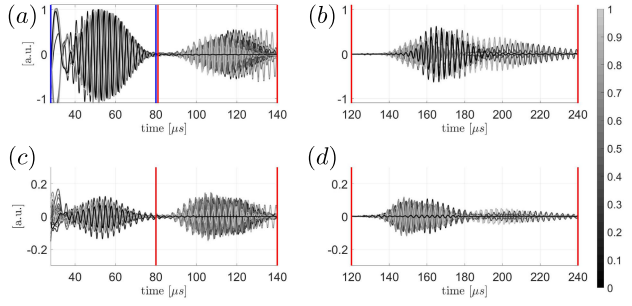

FIGURE 5. Experimental *fully mode-separation* signals for purely SH1 generated at 367 kHz. Reception of the separated SH1 mode (a) and (b) and separated SH0 mode (c) and (d). Reception before the defect, at position (1), (a) and (c) and after the defect, position (2), (b) and (d). The severity of the defects is given by the color bar.

early times, the direct pulse is affected by interference from the high-power excitation signal applied to the EMAT, which is not present in the numerical simulation.

Mode-separation in transmission signals are shown in Fig. 6 and 7 for simulation and experiments, respectively. In this case, a high purity SH1 mode is still generated, but the reflected and transmitted signals have both SH0 and SH1 modes which interfere. Finally, when no mode separation procedure is adopted, *non-separated modes* signals are obtained, as depicted in Fig. 8 and 9 for simulation and experiments, respectively. As can be seen, the shape of the direct pulse differs from previous cases, since the SH1 mode is not the only mode generated.

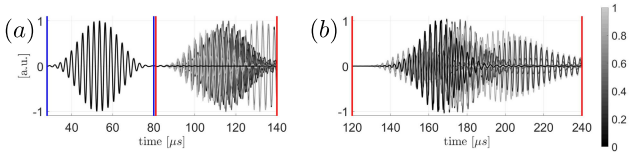

FIGURE 6. Simulated *mode-separation in transmission* signals generated at 367 kHz. Reception before the defect, at position (1), (a) and after the defect, position (2), (b). The severity of the defects is given by the color bar. Note that the *mode-separation in transmission* signals result in a single received signal at each position.

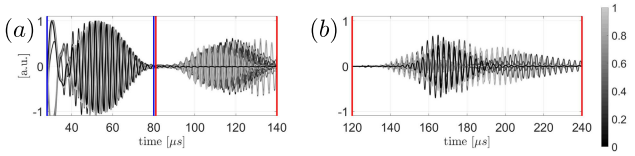

FIGURE 7. Experimental *mode-separation in transmission* signals generated at 367 kHz. The color bar represents the severity of each defect. Reception before the defect, at position (1), (a) and after the defect, position (2), (b).

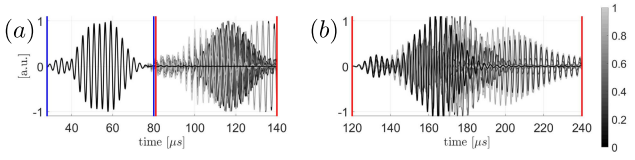

FIGURE 8. Simulated *non-separated modes* signals generated at 367 kHz. Reception before the defect, at position (1), (a) and after the defect, position (2), (b). The color bar represents the severity of the defects.

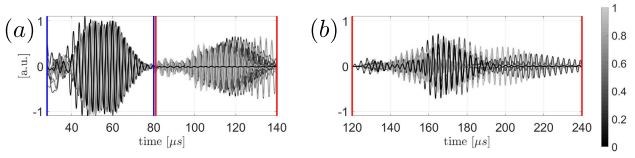

FIGURE 9. Experimental *non-separated modes* signals generated at 367 kHz. Reception before the defect, at position (1), (a) and after the defect, position (2), (b). The severity of the defects is represented by the color bar.

It is worth noting that either *non-separated modes* or *mode-separation in transmission* produce a single received signal at each position, related to the response signal at one surface of the plate, unlike *fully mode-separation*, where two signals are obtained for each generation source. Those relate to a non-mode converted signal and a mode-converted signal, which are only obtained when separation in reception is performed through the sum of responses on the upper and lower surfaces of the plate, see (3). A similar set of signals can be plotted for the generation of the SH0 mode, but are not shown here for the sake of brevity. In order to avoid interference from reflections at the plate's end, a time gate for the reflected and transmitted waves, shown in Fig. 4 to 9 by the red vertical lines, is defined; the blue vertical lines define the incident wave. These gates are defined by the expected arrival time of the reflected and transmitted modes, according to their group speed. Only signals arriving within these gates are used further in the feature extraction procedure, and they will be referred to as patches hereinafter. It is worth mentioning that only the simulated signals that have an experimental counterpart were displayed in Fig. 4, 6, and 8, to facilitate visualization and comparison. All the 1230 cases previously mentioned were used during the construction of the dataset, and consequently in the training of the ML models.

IV. CORROSION-LIKE DEFECTS ESTIMATION METHODS

In the present section, we state the methods used in the overall data-driven modeling construction activity. Fig. 10 summarizes all the steps generally performed for the creation of predictive models. Below we describe each of these steps, together with a description of what was defined in the present work with justifications.

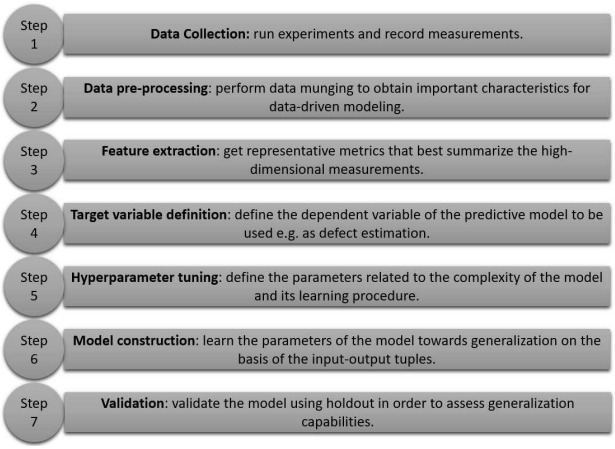

FIGURE 10. Predictive modeling general procedure. The model can be reiterated according to model validation metrics, going back to any of the previous steps. Note that the step-by-step approach gives this recurrence, as the data-driven modeling is inherently iterative.

A. DATA COLLECTION

Data from experiments and simulations are used in the present paper. The former is used to validate the model, while the

latter is used to create it. In the present paper, we show that it is possible to create a data-driven model using simulated data, that can be validated with experiments when the high-fidelity model operates inside the envelope defined by the measurements. The confirmation of such a modeling approach is important, as in many cases data is expensive to measure, making data-intensive predictive modeling for damage estimation non-viable in such scenarios. It is worth highlighting that the computation time for each simulated sample is in the order of few minutes, whereas the whole experimental data acquisition for each sample, including specimen machining and experimentation, can take over one day of work. Details of the FEM model used to generate the training data are provided in Section III, together with the experimental data.

B. PRE-PROCESSING

The raw data that we use for testing the model should be pre-processed, in order to produce valid results when the supervised mathematical model is employed. In this paper, we use data normalization, and we look for the correct time window of interest. We detail each of these pre-processing tasks below.

- Normalization: Considering linearity, we multiplied the measurements by the inverse of the maximum absolute amplitude of each incident wave. In this way, all amplitudes of the transmission and reflection are standardized with no loss of information. The amplitude of experimental and simulated signals differ, mainly due to attenuation, which was not introduced in the numerical simulation. Therefore, the amplitude of the experimental signals was also corrected, based on the same case of the simulated wave signal within the proper time windows.
- Time window: We define the time window that contains relevant information about the transmission and reflection measurements. The goal is to use the time history that is most relevant to the phenomenon at hand.
- Mode separation: three different datasets for data-driven modeling are described in the present work. We constructed different models in order to check whether the mode separation procedure helps to improve the results for defect size estimation in the ML models. The mode separation strategies are defined as (i) *full mode separation*, (ii) *mode separation in transmission*, and (iii) *non-separated*.

C. FEATURE EXTRACTION

A feature extraction process is necessary to reduce the high-dimensionality of the time series in such a way, that the model construction process is possible. The goal is to obtain features that are sensitive to the defect parameters and can be representative of the physical characteristics of received signals in a reduced dimension, when compared to the full amount of samples of the time series, that are subsequently used as inputs for the model [58]. In the present work, we focus on simple feature extraction for signals in the time domain, as it is simpler and less computationally intensive. Table 1 summarizes the features tested in the present work. They have been used elsewhere, mainly in health monitoring applications such as [58], [59], and carry basic time history and statistical information.

TABLE 1. Description of the features used in the scope of the present paper. For all (i)-(iii) strategies of mode separation in the pre-processing, we obtain each of the features described below. They consist of time domain features, as well as simple statistics. By using simple feature engineering, we are able to provide fast yet informative solutions for supervised learning.

Feature Number	Description
1	L_2-energy norm: norm of the vector containing all measurements in a window
2	Curve length
3	Kurtosis
4	Maximum amplitude
5	Number of peaks greater than 60% of the maximum amplitude
6	Number of peaks greater than 20% of the maximum amplitude
7	Mean of peak values greater than 60% of the maximum amplitude
8	Mean of peak values greater than 20% of the maximum amplitude
9	Standard deviation of peak values greater than 60% of the maximum amplitude
10	Standard deviation of peak values greater than 20% of the maximum amplitude
11	Reflection Coefficient: this is calculated by the ratio of the amplitudes of the reflected to the incident waves at the position (1) in Fig.2. Incident and reflected waves are selected by the content of the blue and red gates in Figs.4 to 9. [20], [48]
12	Transmission Coefficient: this is calculated by the ratio of the amplitudes of the wave transmitted through the whole region of the defect to the incident wave at position (2) and (1), respectively, in Fig.2. Incident and transmitted waves are selected by the content of the blue and red gates in Figs.4 to 9. [20], [48].
13	Pearson Coefficient: correlation of the incident and reflected wave

The number of total features depends on each of the cases (i)-(iii) for mode separation. In case (i), the L_2-energy norm, the curve length, the Kurtosis, and the self-explanatory amplitude related features (7 features) are extracted from the 8 patches of signals, resulting in 80 features. Besides those features, the transmission and reflection coefficients culminate in 8 new features. All of those features added to the two Pearson correlation coefficients, yields a total of 90 features. All the features that are previously extracted from the 8 patches in case (i), are obtained for only 4 patches in case (ii) and case (iii), resulting in 40 features in these cases. Recall that case (i) results in two signals for each generation source in each position, as explained in the previous section, whereas cases (ii) and (iii), result in just one signal at each position, thus presenting a different number of patches. Reflection and transmission coefficients add 4 more features, that together with the two Pearson correlation coefficients, sums up to 46 features.

It should be noted that this step is important for ensuring the benefits of the mode separation scheme. It can improve

the ML model construction for defect detection for two main reasons; (i) the presence of multi-modes in the received signals makes the feature extraction step more complicated since more complex signals are generated due to the interference of multi-modes, and (ii) since approximately twice as many signals are available when full mode separation is adopted, additional features are available, and thus richer information is provided to the ML models, so that their overall results are improved.

D. TARGET VARIABLE DEFINITION

We set the target of the model as the damage indices to be predicted on the basis of the guided wave characteristics given in Subsection IV-C. As the definition of whether there is a defect or not can be inferred by only visualization of the SH ultrasonic guided-waves response field, the same cannot be stated in such a specific manner to the severity of the defect. The severity of the defect is measured by the relative area of the thinned defect. Namely, in Fig. 2, the severity of the defect will be given by the area of the trapezoid that varies as a function of α and d normalized per the maximum defect area in the plate.

We perform two types of ML models in the present work, based on the area of the defect:

- Regression: the area of the defects are normalized between [0, 1], which correspond to the minimum and maximum areas, or the nominal condition and largest area of the defect-like corrosion respectively. The normalized values are then used as the target variable.
- Classification: the classification model categorizes the area of the defects into three regions, namely low ($[0, 0.3[$), medium ($[0.3, 0.6[$) and high severity ($[0.6, 1]$).

E. SUPERVISED LEARNING

The extracted features and respective labels representing damage indices (for regression and classification) can be viewed as input-output pairs, which can be employed by any supervised learning, in order to solve the defect estimation problem. In the present work, we solved the regression and classification ML problems with multilayer perceptron artificial neural networks (MLP) and linear models (LM).

The linear model was first adopted in order to check if a simple linear solution could successfully solve the problem, and so assess the difficulty of the damage estimation. We adopted a simple linear regression and linear discriminant analysis for regression and classification problems respectively. Since its performance was not satisfactory, non-linear models with greater prediction capability, such as artificial neural networks were adopted, and turned out to dramatically improve the results. We tested different architectures for the MLPs, a strategy to tune hyperparameters of the model, varying the number of hidden layers and the number of neurons in each of these layers. The number of hidden layers is set from 1 ($\{X\}$) to 3 ($\{X\ X\ X\}$) and the number of neurons in each of these layers as 10 ($X = 10$), 50 ($X = 50$), or 100 ($X = 100$). We adopted a classical multilayer perceptron setup with an MSE loss function, hyperbolic tangent as the activation function in the hidden layers, the output layer for the classification model as a softmax function [59], while for the regression a linear function was used. The scaled conjugate gradient (SCG) backpropagation is adopted as the learning algorithm [60]. The training data were generated by FEM simulations, and in every model construction, 85% of the data were used to train while 15% were used to validate the model, and a stopping criterion was used in order to avoid overfitting. In order to statistically evaluate the results, all the supervised learning models were executed 33 times with different random seeds. Therefore, different optimum weights are found for the many executions and architectures performed. In order to compare different mode separation strategies for feature extraction, we use performance metrics, tailored to evaluate classification and regression problems, namely, accuracy, Kappa coefficient, Confusion Matrix (CM), the Receiver Operating Characteristic (ROC) curve, the area under the ROC curve (AUC), coefficient of determination (R^2), and area under the accuracy curve (AUAC). For details regarding the aforementioned metrics please refer to [59].

V. RESULTS

In the present section, we present the results when applying classification and regression-based supervised learning with linear models and artificial neural networks, to the problem of defect estimation using SH guided waves and mode separation. The presentation of the results is divided in classification and the regression-based solutions, which are explored respectively in Subsections V-A and V-B.

A. CLASSIFICATION RESULTS

'The classification with linear and MLP models was divided according to the mode separation considered as the signal pre-processing methods, namely, (i) *full mode separation*, (ii) *mode separation in transmission*, and (iii) *non-separated* signals. Table 2 reports the results. In case (iii), results achieved by the MLPs are satisfactory, with mean accuracy ranging from 0.73 to 0.81 and best accuracy reaching 0.9118. Results of the case (ii) are also shown. The mean accuracy dropped to a range between 0.69 and 0.80, and the best accuracy remained 0.9118. The latter was not able to improve the results of MLP models, compared to case (iii). Interestingly, the outcomes when SH modes are separated in reception produced the best results, that is after interaction with a defect, case (i). In this case, the best accuracy was actually 0.9706. The range of mean accuracy also improves, varying from 0.79 to 0.85.

Additional metrics were investigated for the best-trained models from each mode separation. When looking at Fig. 11, one can notice the CMs for each case. Case (i) made only one single misclassification, classifying one high severity sample as medium severity. The best-trained models from

TABLE 2. Results in terms of accuracy and Kappa metric for all the classification models tested using the data pre-processing cases (i)-(iii). The improvement concerning the error rate of the nonlinear models compared to the linear ones are 90%, 63%, and 67% for (i) *full mode separation*, (ii) *mode separation in transmission*, and (iii), respectively. When we compare the best models for each mode separation cases (i)-(iii), we have for the error rate 67% improvement in case (i). We can see by the results that the nonlinear models with full mode separation strategy perform better.

Case	Model { Architecture }	Accuracy (train)	Accuracy (test)	Kappa (train)	Kappa (test)	Best accuracy
(i)	MLP {10}	0.9325 ± 0.0177	0.8538 ± 0.0399	0.9010 ± 0.0252	0.7984 ± 0.0699	0.9412
	MLP {50}	0.9219 ± 0.0776	0.8244 ± 0.0800	0.8840 ± 0.1174	0.7526 ± 0.1270	0.9118
	MLP {100}	0.8744 ± 0.1516	0.7888 ± 0.1135	0.8125 ± 0.2287	0.6918 ± 0.1728	0.9118
	MLP {10 10}	0.9225 ± 0.0292	0.8262 ± 0.0501	0.8881 ± 0.0375	0.7558 ± 0.0770	0.9412
	MLP {50 50}	0.9340 ± 0.0210	0.8307 ± 0.0713	0.9030 ± 0.0312	0.7589 ± 0.1034	0.9118
	MLP {100 100}	0.8943 ± 0.0999	0.8111 ± 0.1043	0.8431 ± 0.1503	0.7295 ± 0.1504	0.9412
	MLP {10 10 10}	0.9166 ± 0.0905	0.7995 ± 0.1031	0.8855 ± 0.0926	0.7230 ± 0.1129	0.9412
	MLP {50 50 50}	0.9175 ± 0.0593	0.8084 ± 0.1024	0.8779 ± 0.0923	0.7290 ± 0.1421	**0.9706**
	MLP {100 100 100}	0.9385 ± 0.0160	0.8378 ± 0.0575	0.9087 ± 0.0235	0.7633 ± 0.0894	**0.9706**
	Linear Model	0.7353 ± 0.0044	0.7059 ± 0.0000	0.6025 ± 0.0067	0.5157 ± 0.0000	0.7059
(ii)	MLP {10}	0.9292 ± 0.0272	0.7718 ± 0.0754	0.8948 ± 0.0407	0.6586 ± 0.1069	0.8824
	MLP {50}	0.9102 ± 0.0845	0.7228 ± 0.0754	0.8661 ± 0.1285	0.5858 ± 0.1101	0.8529
	MLP {100}	0.8939 ± 0.1147	0.6916 ± 0.1149	0.8409 ± 0.1737	0.5482 ± 0.1706	0.8529
	MLP {10 10}	0.9282 ± 0.0252	0.7522 ± 0.0739	0.8940 ± 0.0369	0.6370 ± 0.1002	**0.9118**
	MLP {50 50}	0.9353 ± 0.0235	0.7433 ± 0.0675	0.9036 ± 0.0348	0.6229 ± 0.0959	0.8824
	MLP {100 100}	0.8779 ± 0.1398	0.6925 ± 0.0987	0.8171 ± 0.2101	0.5411 ± 0.1626	0.8529
	MLP {10 10 10}	0.9172 ± 0.0296	0.7977 ± 0.0689	0.8782 ± 0.0432	0.6934 ± 0.0978	0.8824
	MLP {50 50 50}	0.9220 ± 0.0641	0.7424 ± 0.0694	0.8838 ± 0.0958	0.6171 ± 0.1072	0.8824
	MLP {100 100 100}	0.8863 ± 0.1097	0.7193 ± 0.1125	0.8295 ± 0.1661	0.5829 ± 0.1642	0.8824
	Linear Model	0.7987 ± 0.0039	0.7647 ± 0.0000	0.7021 ± 0.0056	0.6180 ± 0.0000	0.7647
(iii)	MLP {10}	0.9009 ± 0.0471	0.7888 ± 0.0651	0.8532 ± 0.0724	0.6792 ± 0.0862	0.8529
	MLP {50}	0.8985 ± 0.0575	0.8128 ± 0.0514	0.8519 ± 0.0703	0.7162 ± 0.0815	**0.9118**
	MLP {100}	0.8655 ± 0.1185	0.7754 ± 0.0685	0.7996 ± 0.1781	0.6503 ± 0.1163	0.8824
	MLP {10 10}	0.9042 ± 0.0381	0.7977 ± 0.0408	0.8607 ± 0.0553	0.6898 ± 0.0652	0.8529
	MLP {50 50}	0.9204 ± 0.0548	0.7923 ± 0.0674	0.8831 ± 0.0795	0.6841 ± 0.1042	**0.9118**
	MLP {100 100}	0.8744 ± 0.1009	0.7638 ± 0.0905	0.8120 ± 0.1540	0.6422 ± 0.1319	**0.9118**
	MLP {10 10 10}	0.8835 ± 0.0638	0.7754 ± 0.0601	0.8314 ± 0.0911	0.6546 ± 0.0895	0.8824
	MLP {50 50 50}	0.8758 ± 0.0988	0.7308 ± 0.0965	0.8161 ± 0.1483	0.5904 ± 0.1412	0.8529
	MLP {100 100 100}	0.8596 ± 0.1196	0.7389 ± 0.1083	0.7897 ± 0.1804	0.6034 ± 0.1564	0.8824
	Linear Model	0.7969 ± 0.0041	0.7353 ± 0.0000	0.6997 ± 0.0059	0.5591 ± 0.0000	0.7353

TABLE 3. Performance metrics for the best cases of each mode separation. Rates such as the TPR and FPR are depicted for each class and considering a macro and micro average. Case (i) obtains the best rates in every class and in both types of average considered.

Class	Rate	Case (i)	Case (ii)	Case (iii)
Low	TPR	1.0000	0.8750	0.8750
	FPR	0.0000	0.0000	0.0000
Medium	TPR	1.0000	1.0000	1.0000
	FPR	0.0417	0.1250	0.1250
High	TPR	0.9375	0.8750	0.8750
	FPR	0.0000	0.0000	0.0000
Macro Avg.	TPR	0.9792	0.9167	0.9167
	FPR	0.0139	0.0417	0.0417
Micro Avg.	TPR	0.9706	0.9118	0.9118
	FPR	0.0147	0.0441	0.0441

cases (ii) and (iii) missed two additional samples, stemming from the low severity class and the high severity one. It is important to compare the CMs rates in order to average values from all the classes. Table 3 depicts the True Positive Rate (TPR) and False Positive Rate (FPR) from all the classes and, also, displays two types of average. The macro average considers a simple average of the results from all classes, while the micro average takes into account the true positives, false positives, true negatives, and false negatives of each individual class. The latter is more adequate to unbalanced datasets which is the current situation. As we can see, case (i) has the greatest TPR in every class and every type of average as well as the lowest FPR. Cases (ii) and (iii) have similar results as expected, since both models missed samples from the same classes. Finally, one can also observe the ROC curves and AUC for the best cases in Fig. 12. ROC curves for each class and micro and macro averages are shown in Fig. 12(a) to 12(c) representing cases (i) to (iii), respectively. It is important to mention that the closer the AUC is to 1, the better. The lower its value is, the closer the curve is to a random classifier (AUC $\approx$ 0.5, represented by the dotted black diagonal line). Case (i) is shown to have the best AUC in all classes, with the exception of the high severity. Case (ii) obtained considerably worse results overall. Looking at Fig. 12(d), we can observe the micro average AUC from every case overlapped. When considering the AUC and ROC metrics, case (i) still yields the best performance. This indicates that the mode conversion phenomenon, and the consequent mode-mixing of converted modes, indeed produce received signals that are more complex to analyse. When the modes are fully separated, the analysis is simplified and better results may be achieved as we have shown.

Concerning the tuning of the architecture of the models, no specific number of neurons or number of layers generally obtains the best results. However, according to the best mode separation, case (i), a single layer with 10 neurons, and an MLP with three hidden layers with 50 or 100 neurons are the

Actual \ Predicted	L	M	H
L	1.00 (8)	0.00 (0)	0.00 (0)
M	0.00 (0)	1.00 (10)	0.00 (0)
H	0.00 (0)	0.06 (1)	0.94 (15)

(a)

Actual \ Predicted	L	M	H
L	0.88 (7)	0.12 (1)	0.00 (0)
M	0.00 (0)	1.00 (10)	0.00 (0)
H	0.00 (0)	0.12 (2)	0.88 (14)

(b)

Actual \ Predicted	L	M	H
L	0.88 (7)	0.12 (1)	0.00 (0)
M	0.00 (0)	1.00 (10)	0.00 (0)
H	0.00 (0)	0.12 (2)	0.88 (14)

(c)

FIGURE 11. CMs for the best cases in all mode separations. (a) case (i), (b) case (ii), and (c) case (iii). Notice that cases (ii) and (iii) present similar CMs.

best architectures to adopt, obtaining the best mean accuracy and the best single accuracy respectively. The train results are mostly greater than the test results in all cases. This is expected since the data used is in fact the same utilized to train the model, that is, the simulated signals.

Lastly, regarding the Kappa coefficient, all the models showed at least, reasonable results. All results were greater than 0.5, which validates the fairness of the models. Looking at the linear model accuracy, one can conclude that the results are not satisfactory when compared to the nonlinear models based on MLPs, regardless of the pre-processing cases (i)-(iii). We kept the results of the linear model, to compare the MLP to a baseline and illustrate some of the difficulties with the present case study. In the following, we check the results of the regression models for defect estimation.

B. REGRESSION RESULTS

Concerning the results achieved by the regression models, the outcome is reported in Table 4. Case (iii) presents the best R^2 and AUAC, respectively, as 0.9089 and 0.9356, while the mean AUAC falls in a range from 0.84 to 0.90. The architecture has a major role in the mean R^2, as different MLPs imply a higher standard deviation for this metric. Case (ii) reports results slightly different from case (iii). The best R^2 is 0.8953 and the best AUAC corresponds to 0.9285. In case (i) signals, results are far superior to the ones attained by (ii) and (iii), especially when we address the mean results of AUC and R^2. Results show, once again, that the mode separation only in transmission is not sufficient to improve ML results. Mode-mixing originated from signals' interactions with the defects still occurs, regardless of if a single guided-wave mode is excited. Therefore, full mode separation is the only

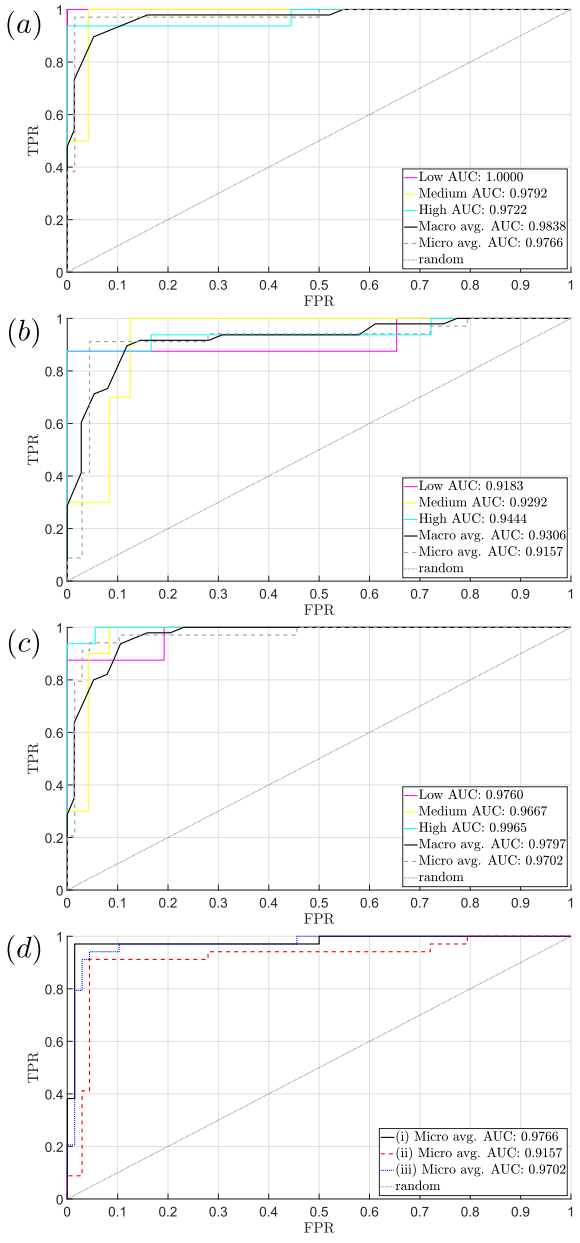

FIGURE 12. ROC curves for the best models from all mode separation cases. Boxes (a), (b), and (c) present the ROC curves and AUC for all classes jointly with their micro and macro averages for the cases (i), (ii), and (iii), respectively. Box (d) presents the micro average ROC curves and AUC of all the mode separation cases. The micro average is the most adequate in this case since the testing dataset is unbalanced.

separation procedure that actually facilitates the supervised learning action. The mean R^2 achieved 0.8196, while the mean AUC reached 0.9222. The best AUAC of the signals is equivalent to 0.9486 and the best R^2 is equal to 0.9211. The linear regression gave poor results when compared to the ones that originated from the MLPs, regardless of the mode separation. When we look at the architecture hyperparameters, it is observed that different specific numbers of neurons and hidden layers are the most adequate for each case. However, the best results are obtained with case (i),

TABLE 4. Results in terms of R^2 and AUAC for all the regression models tested using the data cases (i)-(iii). Looking at the best R^2 and AUAC, case (i) obtained the greatest result, 0.9211 and 0.9486 respectively. Once again, another indication that the nonlinear models with full mode separation achieve the greatest performance.

Case	Model { Architecture }	R^2 (train)	R^2 (test)	Best R^2	AUAC (train)	AUAC (test)	Best AUAC
(i)	MLP {10}	0.9783 ± 0.0040	0.7910 ± 0.0710	0.9045	0.9727 ± 0.0031	0.9201 ± 0.0140	0.9456
	MLP {50}	0.9710 ± 0.0155	0.3685 ± 0.4015	0.7667	0.9678 ± 0.0081	0.8645 ± 0.0301	0.9199
	MLP {100}	0.9644 ± 0.0288	-0.2655 ± 0.7682	0.8282	0.9646 ± 0.0114	0.8302 ± 0.0464	0.9128
	MLP {10 10}	0.9787 ± 0.0057	0.7989 ± 0.0935	0.9122	0.9729 ± 0.0040	0.9174 ± 0.0163	0.9435
	MLP {50 50}	0.9751 ± 0.0130	0.2909 ± 0.8652	0.8709	0.9708 ± 0.0080	0.8848 ± 0.0327	0.9356
	MLP {100 100}	0.9567 ± 0.0543	-0.0937 ± 0.8140	0.6625	0.9627 ± 0.0168	0.8432 ± 0.0341	0.9080
	MLP {10 10 10}	0.9792 ± 0.0070	0.8196 ± 0.1029	0.9211	0.9734 ± 0.0051	0.9222 ± 0.0131	**0.9486**
	MLP {50 50 50}	0.9744 ± 0.0110	0.6357 ± 0.3080	0.8944	0.9704 ± 0.0069	0.8978 ± 0.0189	0.9314
	MLP {100 100 100}	0.9676 ± 0.0199	0.3881 ± 0.4419	0.8378	0.9665 ± 0.0100	0.8640 ± 0.0398	0.9160
	Linear Regression	0.9690 ± 0.0007	-3.9921 ± 0.0000	-3.9921	0.9649 ± 0.0004	0.6405 ± 0.0000	0.6405
(ii)	MLP {10}	0.9650 ± 0.0172	0.5248 ± 0.2795	0.7884	0.9644 ± 0.0094	0.8658 ± 0.0357	0.9025
	MLP {50}	0.9625 ± 0.0164	0.3037 ± 0.2094	0.7267	0.9629 ± 0.0086	0.8438 ± 0.0275	0.8818
	MLP {100}	0.9596 ± 0.0318	-0.2161 ± 0.4026	0.5513	0.9627 ± 0.0129	0.8103 ± 0.0375	0.8668
	MLP {10 10}	0.9710 ± 0.0137	0.5873 ± 0.1225	0.8953	0.9681 ± 0.0076	0.8759 ± 0.0196	**0.9285**
	MLP {50 50}	0.9691 ± 0.0237	0.3726 ± 0.1994	0.7022	0.9672 ± 0.0106	0.8617 ± 0.0251	0.8940
	MLP {100 100}	0.9642 ± 0.0159	-0.1449 ± 0.5016	0.6656	0.9637 ± 0.0085	0.8185 ± 0.0405	0.8844
	MLP {10 10 10}	0.9698 ± 0.0149	0.6079 ± 0.1276	0.7939	0.9675 ± 0.0078	0.8823 ± 0.0171	0.9131
	MLP {50 50 50}	0.9611 ± 0.0308	0.4563 ± 0.2268	0.7824	0.9630 ± 0.0119	0.8621 ± 0.0271	0.9062
	MLP {100 100 100}	0.9613 ± 0.0446	0.1292 ± 0.4091	0.6869	0.9642 ± 0.0149	0.8426 ± 0.0304	0.8861
	Linear Regression	0.9435 ± 0.0014	0.4404 ± 0.0000	0.4404	0.9520 ± 0.0005	0.8218 ± 0.0000	0.8218
(iii)	MLP {10}	0.9618 ± 0.0153	0.7590 ± 0.0864	0.8692	0.9635 ± 0.0077	0.8999 ± 0.0169	0.9266
	MLP {50}	0.9625 ± 0.0198	0.5767 ± 0.2197	0.8541	0.9636 ± 0.0097	0.8726 ± 0.0252	0.9168
	MLP {100}	0.9515 ± 0.0292	0.2572 ± 0.2838	0.7312	0.9585 ± 0.0124	0.8354 ± 0.0288	0.8940
	MLP {10 10}	0.9579 ± 0.0289	0.7598 ± 0.0732	0.9089	0.9629 ± 0.0133	0.9019 ± 0.0122	**0.9356**
	MLP {50 50}	0.9700 ± 0.0120	0.5888 ± 0.2796	0.8338	0.9678 ± 0.0068	0.8767 ± 0.0261	0.9155
	MLP {100 100}	0.9564 ± 0.0312	0.1509 ± 0.6388	0.6811	0.9610 ± 0.0115	0.8475 ± 0.0294	0.8905
	MLP {10 10 10}	0.9576 ± 0.0265	0.7383 ± 0.0946	0.8692	0.9629 ± 0.0125	0.8974 ± 0.0180	0.9238
	MLP {50 50 50}	0.9647 ± 0.0253	0.6582 ± 0.1299	0.8706	0.9659 ± 0.0115	0.8864 ± 0.0156	0.9231
	MLP {100 100 100}	0.9644 ± 0.0140	0.5295 ± 0.1653	0.7362	0.9642 ± 0.0075	0.8628 ± 0.0212	0.8918
	Linear Regression	0.9401 ± 0.0012	0.5558 ± 0.0000	0.5558	0.9515 ± 0.0005	0.8450 ± 0.0000	0.8450

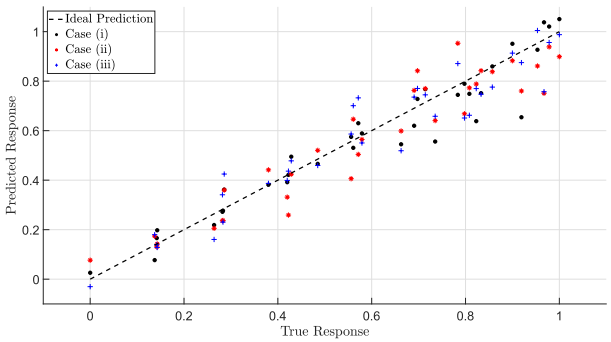

FIGURE 13. Best test results for true versus predicted response. Note that results of case (i), achieved by the MLP { 10 10 10 }, are closer to the dashed line, which represents ideal prediction ($R^2 = 1$).

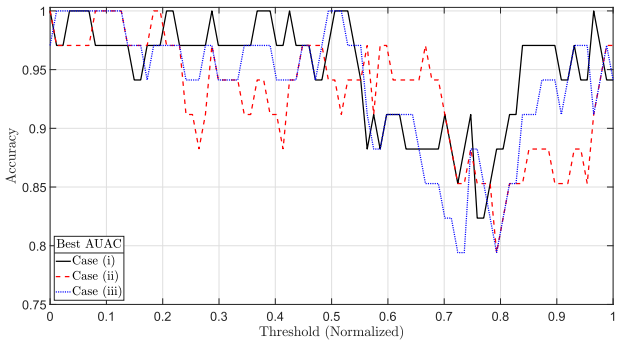

FIGURE 14. Best test results for the AUAC of the best cases from all (i)-(iii) mode separations. One can infer that the curve achieved by case (i) is the one closer to unity.

an MLP with 100 neurons jointly with 3 hidden layers. The train results are greater than the test ones which is as expected, remembering that the same occurred in the aforementioned classification results.

The R^2 metric and its performance is highlighted in Fig. 13. The correlation between prediction and true response is observed, and the best cases of all the datasets are presented. It is notable how case (i) results, obtained in the {10 10 10} MLP architecture, are closer to the ideal prediction, $R^2 = 1$, which is shown by the dashed black line. The closer the data is to the line, the higher the R^2. The AUAC of the best cases of the three datasets are also presented in Fig. 14. Notice how the AUAC of (i) encompasses most of the graph, while (ii) and (iii) cover a smaller area.

Finally, the classification results can be compared to the regression results. When comparing the error rate between the classification accuracy and the regression AUAC, it is seen that the case (i) dataset achieves a 67% error rate improvement, while the error rate of the regression AUAC drops by 30% with the mode separation treatment. In the classification, the data is classified as three different outputs (low, medium, and high severity), whilst regression treats the

data as a continuous output. The choice on which approach is used depends on whether fine monitoring must be employed or categorical output is sufficient. In the former, a regression would be recommended, whereas, in the latter, a classification strategy suffices. The regression strategy did yield reasonable results, $R^2 = 0.9211$. Results have shown that a 97.06% accuracy is found using classification with full mode separation.

VI. CONCLUSION

In this paper, ultrasonic signals due to the interaction of SH ultrasonic guided waves with corrosion-like defects in plates were applied to supervised ML algorithms for defect estimation. In the frequency-thickness product range considered for this work, only either the SH0 or SH1 modes can propagate. They are thus mixed in the time and frequency domain. Additionally, the individual behaviour of each mode is complex when interacting with the defect, which includes mode-conversion. These characteristics motivated the application of ML techniques. Moreover, we have investigated whether the estimation of the defect is facilitated and improved if one can remove the effect of mode-mixing. A baseline-free data-driven model was proposed and different damage indices for the defect, such as continuous and discrete, were studied. Both numerical and experimental signals were used, such that the former served to train the model and the latter to test it. We have shown that the full mode separation strategy jointly with the SHM methodology proposed, has indeed significantly improved the performance of the data-driven models, since mode-mixing, mainly of converted modes, produced complicated signals. When full mode separation is applied, the error rate decreases by 30% and 67% in the regression-based and classification-based models, respectively. It is also worth noting that based on the obtained results, the adopted strategy of restricting simulated data to train the model and the use of experimental data to validate it was an effective approach, and that the fidelity of the simulated signals, shown in Fig. 4 to 9, was high enough not to impose significant feature loss when compared to experimental signals.

The results achieved demonstrate the potential this new technique of analysing SH wave modes interacting with defects to determine defect size. Future work suggestions would include comparing the mode separation performance with more parameters, such as varying the position and length of the defect, which is already discussed in the literature with pipes and plates [37], [61]. Another area for future work is the feature engineering process. Additional feature extraction methodologies such as principal component analysis (PCA) [62], linear and non-linear auto-regressive models [63], and frequency-based features [59] can be explored. In addition, the importance and ranking of the features can also be explored [64], [65]. By using decision tree methods or random cross-validation with different features combinations, one could rank the most important features, and use these to inform the approach taken, saving time and providing simpler solutions. From the ML viewpoint, a data augmentation approach [41], [66] can be addressed for both the simulated and experimental datasets of this work. Another approach would be addressing each of the mode separation datasets with automatic feature extraction - in other words DL techniques [39] that could use for example convolutional neural networks [40], [41].

REFERENCES

[1] M. Clough, M. Fleming, and S. Dixon, "Circumferential guided wave EMAT system for pipeline screening using shear horizontal ultrasound," *NDT E Int.*, vol. 86, pp. 20–27, Mar. 2017.

[2] A. Demma, P. Cawley, M. Lowe, A. G. Roosenbrand, and B. Pavlakovic, "The reflection of guided waves from notches in pipes: A guide for interpreting corrosion measurements," *NDT E Int.*, vol. 37, no. 3, pp. 167–180, Apr. 2004.

[3] S. Wang, S. Huang, W. Zhao, and Z. Wei, "3D modeling of circumferential SH guided waves in pipeline for axial cracking detection in ILI tools," *Ultrasonics*, vol. 56, pp. 325–331, Feb. 2015.

[4] A. Demma, P. Cawley, and M. Lowe, "Scattering of the fundamental shear horizontal mode from steps and notches in plates," *J. Acoust. Soc. Amer.*, vol. 113, no. 4, pp. 1880–1891, Apr. 2003.

[5] M. Hirao and H. Ogi, "An SH-wave EMAT technique for gas pipeline inspection," *NDT E Int.*, vol. 32, no. 3, pp. 127–132, Apr. 1999.

[6] H. Zhang, Y. Du, J. Tang, G. Kang, and H. Miao, "Circumferential SH wave piezoelectric transducer system for monitoring corrosion-like defect in large-diameter pipes," *Sensors*, vol. 20, no. 2, p. 460, Jan. 2020.

[7] W. Zhang, H. Hao, J. Wu, J. Li, H. Ma, and C. Li, "Detection of minor damage in structures with guided wave signals and nonlinear oscillator," *Measurement*, vol. 122, pp. 532–544, Jul. 2018.

[8] D. J. Thomson, N. Durham, K. Abdel-Hadi, C. A. McKenzie, and J. Zhao, "Acoustic guided wave techniques for detecting corrosion damage of electrical grounding rods," *Measurement*, vol. 147, Dec. 2019, Art. no. 106858.

[9] Y. Wang and X. Li, "Propagation characteristics and defect sensitivity analysis of guided wave from single excitation source in elbows," *IEEE Access*, vol. 7, pp. 75542–75549, 2019.

[10] W. J. Staszewski, *Structural Health Monitoring Using Guided Ultrasonic Waves*. Heidelberg, Germany: Springer, 2004, ch. 6, pp. 117–162.

[11] L. Mallet, B. C. Lee, W. J. Staszewski, and F. Scarpa, "Structural health monitoring using scanning laser vibrometry: II. Lamb waves for damage detection," *Smart Mater. Struct.*, vol. 13, no. 2, pp. 261–269, Feb. 2004.

[12] S. Pavlopoulou, W. J. Staszewski, and C. Soutis, "Evaluation of instantaneous characteristics of guided ultrasonic waves for structural quality and health monitoring," *Struct. Control Health Monitor.*, vol. 20, no. 6, pp. 937–955, Jun. 2013.

[13] K. Dziedziech, L. Pieczonka, P. Kijanka, and W. J. Staszewski, "Enhanced nonlinear crack-wave interactions for structural damage detection based on guided ultrasonic waves," *Struct. Control Health Monitor.*, vol. 23, no. 8, pp. 1108–1120, Aug. 2016.

[14] M. Mitra and S. Gopalakrishnan, "Guided wave based structural health monitoring: A review," *Smart Mater. Struct.*, vol. 25, no. 5, May 2016, Art. no. 053001.

[15] R. Radecki, Z. Su, L. Cheng, P. Packo, and W. J. Staszewski, "Modelling nonlinearity of guided ultrasonic waves in fatigued materials using a nonlinear local interaction simulation approach and a spring model," *Ultrasonics*, vol. 84, pp. 272–289, Mar. 2018.

[16] B. S. Ben, B. A. Ben, K. A. Vikram, and S. H. Yang, "Damage identification in composite materials using ultrasonic based Lamb wave method," *Measurement*, vol. 46, no. 2, pp. 904–912, Feb. 2013.

[17] X. Qin, S. Zhang, C. Xu, J. Xie, G. Chen, and G. Song, "Detection of surface breaking cracks filled with solid impurities using a baseline-free NEWS-TR method," *IEEE Access*, vol. 8, pp. 56908–56920, 2020.

[18] M. Hirao and H. Ogi, *EMATs for Science and Industry: Noncontacting Ultrasonic Measurements*. Amsterdam, The Netherlands: Springer, 2003.

[19] R. Carandente, J. Ma, and P. Cawley, "The scattering of the fundamental torsional mode from axi-symmetric defects with varying depth profile in pipes," *J. Acoust. Soc. Amer.*, vol. 127, no. 6, pp. 3440–3448, Jun. 2010.

[20] A. C. Kubrusly, M. A. Freitas, J. P. von der Weid, and S. Dixon, "Interaction of SH guided waves with wall thinning," *NDT E Int.*, vol. 101, pp. 94–103, Jan. 2019.

[21] A. Dhutti, S. A. Tumin, W. Balachandran, J. Kanfoud, and T.-H. Gan, "Development of ultrasonic guided wave transducer for monitoring of high temperature pipelines," *Sensors*, vol. 19, no. 24, p. 5443, Dec. 2019.
[22] B. Vogelaar, G. Priems, K. Bourgonje, and M. Golombok, "Time-lapse acoustic monitoring of deteriorating pipes," *Struct. Health Monitor.*, vol. 18, nos. 5–6, pp. 1995–2003, Nov. 2019.
[23] S. Mariani, S. Heinlein, and P. Cawley, "Compensation for temperature-dependent phase and velocity of guided wave signals in baseline subtraction for structural health monitoring," *Struct. Health Monitor.*, vol. 19, no. 1, pp. 26–47, Jan. 2020.
[24] G. Shkerdin and C. Glorieux, "Lamb mode conversion in a plate with a delamination," *J. Acoust. Soc. Amer.*, vol. 116, no. 4, pp. 2089–2100, Oct. 2004.
[25] L. Moreau, M. Castaings, B. Hosten, and M. V. Predoi, "An orthogonality relation-based technique for post-processing finite element predictions of waves scattering in solid waveguides," *J. Acoust. Soc. Amer.*, vol. 120, no. 2, pp. 611–620, Aug. 2006.
[26] Nurmalia, N. Nakamura, H. Ogi, and M. Hirao, "Detection of shear horizontal guided waves propagating in aluminum plate with thinning region," *Jpn. J. Appl. Phys.*, vol. 50, no. 7, 2011, Art. no. 07HC17.
[27] Nurmalia, N. Nakamura, H. Ogi, M. Hirao, and K. Nakahata, "Mode conversion behavior of SH guided wave in a tapered plate," *NDT E Int.*, vol. 45, no. 1, pp. 156–161, Jan. 2012.
[28] Nurmalia, N. Nakamura, H. Ogi, and M. Hirao, "Mode conversion and total reflection of torsional waves for pipe inspection," *Jpn. J. Appl. Phys.*, vol. 52, no. 7, 2013, Art. no. 07HC14.
[29] A. Pau, D. V. Achillopoulou, and F. Vestroni, "Scattering of guided shear waves in plates with discontinuities," *NDT E Int.*, vol. 84, pp. 67–75, Dec. 2016.
[30] A. Pau and D. V. Achillopoulou, "Interaction of shear and Rayleigh–Lamb waves with notches and voids in plate waveguides," *Materials*, vol. 10, no. 7, p. 841, 2017.
[31] A. C. Kubrusly, J. P. von der Weid, and S. Dixon, "Experimental and numerical investigation of the interaction of the first four SH guided wave modes with symmetric and non-symmetric discontinuities in plates," *NDT E Int.*, vol. 108, Dec. 2019, Art. no. 102175.
[32] P. A. Petcher and S. Dixon, "Mode mixing in shear horizontal ultrasonic guided waves," *Nondestruct. Test. Eval.*, vol. 32, no. 2, pp. 113–132, 2017.
[33] C.-T. Ng, "On the selection of advanced signal processing techniques for guided wave damage identification using a statistical approach," *Eng. Struct.*, vol. 67, pp. 50–60, May 2014.
[34] M. Kuhn and K. Johnson, *Applied Predictive Modeling*. New York, NY, USA: Springer, 2013.
[35] H. Salehi and R. Burgueño, "Emerging artificial intelligence methods in structural engineering," *Eng. Struct.*, vol. 171, pp. 170–189, Sep. 2018.
[36] G. Dib, O. Karpenko, E. Koricho, A. Khomenko, M. Haq, and L. Udpa, "Ensembles of novelty detection classifiers for structural health monitoring using guided waves," *Smart Mater. Struct.*, vol. 27, no. 1, Nov. 2017, Art. no. 015003.
[37] J. García-Gómez, R. Gil-Pita, M. Rosa-Zurera, A. Romero-Camacho, J. Jiménez-Garrido, and V. García-Benavides, "Smart sound processing for defect sizing in pipelines using EMAT actuator based multi-frequency Lamb waves," *Sensors*, vol. 18, no. 3, p. 802, Mar. 2018.
[38] S. Yaacoubi, M. E. Mountassir, M. Ferrari, and F. Dahmene, "Measurement investigations in tubular structures health monitoring via ultrasonic guided waves: A case of study," *Measurement*, vol. 147, Dec. 2019, Art. no. 106800.
[39] Y. LeCun, Y. Bengio, and G. Hinton, "Deep learning," *Nature*, vol. 521, pp. 436–444, May 2015.
[40] J. Melville, K. S. Alguri, C. Deemer, and J. B. Harley, "Structural damage detection using deep learning of ultrasonic guided waves," in *Proc. AIP Conf.*, 2018, vol. 1949, no. 1, Art. no. 230004.
[41] V. Ewald, R. M. Groves, and R. Benedictus, "DeepSHM: A deep learning approach for structural health monitoring based on guided Lamb wave technique," in *Proc. Sensors Smart Struct. Technol. Civil, Mech., Aerosp. Syst.*, vol. 10970, Mar. 2019, Art. no. 109700.
[42] D. F. Hesser, G. K. Kocur, and B. Markert, "Active source localization in wave guides based on machine learning," *Ultrasonics*, vol. 106, Aug. 2020, Art. no. 106144.
[43] H. Sun, L. Peng, S. Wang, S. Huang, and K. Qu, "Development of frequency-mixed point-focusing shear horizontal guided-wave EMAT for defect inspection using deep neural network," *IEEE Trans. Instrum. Meas.*, vol. 70, pp. 1–14, 2021.
[44] A. J. Dawson, J. E. Michaels, and T. E. Michaels, "Isolation of ultrasonic scattering by wavefield baseline subtraction," *Mech. Syst. Signal Process.*, vols. 70–71, pp. 891–903, Mar. 2016.
[45] A. J. Croxford, G. Konstantinidis, B. W. Drinkwater, and P. D. Wilcox, "Strategies for guided-wave structural health monitoring," *Proc. Roy. Soc. A, Math. Phys. Eng. Sci.*, vol. 463, no. 2087, pp. 2961–2981, Nov. 2007.
[46] Y. Lu and J. E. Michaels, "A methodology for structural health monitoring with diffuse ultrasonic waves in the presence of temperature variations," *Ultrasonics*, vol. 43, no. 9, pp. 717–731, Oct. 2005.
[47] J. L. Rose, *Ultrasonic Guided Waves in Solid Media*. Cambridge, U.K.: Cambridge Univ. Press, 2014.
[48] A. C. Kubrusly, M. A. Freitas, J. P. von der Weid, and S. Dixon, "Dataset on reflection and transmission coefficients of ultrasonic shear horizontal guided waves in plates with wall thinning," *Data Brief*, vol. 21, pp. 2179–2191, Dec. 2018.
[49] S. Hill and S. Dixon, "Frequency dependent directivity of periodic permanent magnet electromagnetic acoustic transducers," *NDT E Int.*, vol. 62, pp. 137–143, Mar. 2014.
[50] S. Dixon, P. A. Petcher, Y. Fan, D. Maisey, and P. Nickolds, "Ultrasonic metal sheet thickness measurement without prior wave speed calibration," *J. Phys. D, Appl. Phys.*, vol. 46, no. 44, Nov. 2013, Art. no. 445502.
[51] P. A. Petcher, S. E. Burrows, and S. Dixon, "Shear horizontal (SH) ultrasound wave propagation around smooth corners," *Ultrasonics*, vol. 54, no. 4, pp. 997–1004, Apr. 2014.
[52] D. Alleyne and P. Cawley, "A two-dimensional Fourier transform method for the measurement of propagating multimode signals," *J. Acoust. Soc. Amer.*, vol. 89, no. 3, pp. 1159–1168, Mar. 1991.
[53] S. Wang, S. Huang, Q. Wang, Y. Zhang, and W. Zhao, "Mode identification of broadband Lamb wave signal with squeezed wavelet transform," *Appl. Acoust.*, vol. 125, pp. 91–101, Oct. 2017.
[54] G.-F. Zhai and Y.-Q. Li, "Single SH guided wave mode generation method for PPM EMATs," *Chin. Phys. B*, vol. 29, no. 5, May 2020, Art. no. 054303.
[55] P. Khalili and F. Cegla, "Excitation of single-mode shear-horizontal guided waves and evaluation of their sensitivity to very shallow crack-like defects," *IEEE Trans. Ultrason., Ferroelectr., Freq. Control*, vol. 68, no. 3, pp. 818–828, Mar. 2021.
[56] A. C. Kubrusly, M. A. Freitas, J. P. von der Weid, and S. Dixon, "Mode selectivity of SH guided waves by dual excitation and reception applied to mode conversion analysis," *IEEE Trans. Ultrason., Ferroelectr., Freq. Control*, vol. 65, no. 7, pp. 1239–1249, Jul. 2018.
[57] G. Qiu, X. Song, X. Zhang, J. Tu, and T. Chen, "Pure SH1 guided-wave generation method with dual periodic-permanent-magnet electromagnetic acoustic transducers for plates inspection," *Sensors*, vol. 19, no. 13, p. 3019, Jul. 2019.
[58] C. Farrar and K. Worden, *Structural Health Monitoring: A Machine Learning Perspective*. Hoboken, NJ, USA: Wiley, 2013.
[59] Y. Ying, J. H. Garrett, I. J. Oppenheim, L. Soibelman, J. B. Harley, J. Shi, and Y. Jin, "Toward data-driven structural health monitoring: Application of machine learning and signal processing to damage detection," *J. Comput. Civil Eng.*, vol. 27, no. 6, pp. 667–680, Nov. 2013.
[60] M. F. Møller, "A scaled conjugate gradient algorithm for fast supervised learning," *Neural Netw.*, vol. 6, no. 4, pp. 525–533, Jan. 1993.
[61] S. Liu, C. Du, J. Mou, L. Martua, J. Zhang, and F. L. Lewis, "Diagnosis of structural cracks using wavelet transform and neural networks," *NDT E Int.*, vol. 54, pp. 9–18, Mar. 2013.
[62] D. Sen, A. Aghazadeh, A. Mousavi, S. Nagarajaiah, R. Baraniuk, and A. Dabak, "Data-driven semi-supervised and supervised learning algorithms for health monitoring of pipes," *Mech. Syst. Signal Process.*, vol. 131, pp. 524–537, Sep. 2019.
[63] M. G. de Castro Ribeiro, A. C. Kubrusly, and H. V. H. Ayala, "Damage detection in composite plates with ultrasonic guided-waves and nonlinear system identification," in *Proc. IEEE Symp. Ser. Comput. Intell. (SSCI)*, Dec. 2020, pp. 2039–2046.
[64] L. Hussain, W. Aziz, I. R. Khan, M. H. Alkinani, and J. S. Alowibdi, "Machine learning based congestive heart failure detection using feature importance ranking of multimodal features," *Math. Biosci. Eng.*, vol. 18, no. 1, pp. 69–91, 2021.
[65] M. V. García and J. L. Aznarte, "Shapley additive explanations for NO_2 forecasting," *Ecol. Informat.*, vol. 56, Mar. 2020, Art. no. 101039.
[66] T. Hu, T. Tang, and M. Chen, "Data simulation by resampling—A practical data augmentation algorithm for periodical signal analysis-based fault diagnosis," *IEEE Access*, vol. 7, pp. 125133–125145, 2019.

MATEUS GHEORGHE DE CASTRO RIBEIRO was born in 1994. He received the B.S. degree in mechanical engineering from the Federal University of Juiz de Fora, Juiz de Fora, Brazil, in 2018, and the M.S. degree in mechanical engineering from the Pontifical Catholic University of Rio de Janeiro (PUC-Rio), Rio de Janeiro, Brazil, in 2020. He is currently working as an Research and Development Engineer with the Laboratorio de Sensores a Fibras Opticas (LSFO), Department of Mechanical Engineering, PUC-Rio, where his main work is focused on solutions for structural health monitoring based on ultrasonic guided waves jointly with signal processing and machine learning techniques. His research interests include machine learning, ultrasonic waves, signal processing, and structural health monitoring.

ALAN CONCI KUBRUSLY received the degree in electronics and telecommunications engineering, the M.S. degree in electrical engineering, and the Ph.D. degree in mechanical engineering from the Pontifical Catholic University of Rio de Janeiro (PUC-Rio), in 2009, 2012, and 2016, respectively. He has been a Faculty Member with the Centre for Telecommunication Studies, PUC-Rio, since 2016. His current research interests include applications of ultrasound in nondestructive evaluation, guided waves, signal processing, and instrumentation.

HELON VICENTE HULTMANN AYALA was born in 1986. He received the B.S. degree in control and automation engineering from the Pontifical Catholic University of Paraná (PUCPR), in 2009, the dual M.S. degree in advanced robotics from the Warsaw University of Technology and the University of Genoa, in 2012, and the Ph.D. degree in industrial and system engineering from PUCPR, in 2016. He worked as an Undergraduate Intern with ZF Friedrichshafen AG, Germany, a Product Development Engineer with Embraer SA (Brazilian aircraft manufacturer), and a Research Staff Member with the IBM Research Brazil Laboratory. In 2018, he joined the Department of Mechanical Engineering, Pontifical Catholic University of Rio de Janeiro, where he is currently serving as a Professor Adjunto. His research interests include system identification, advanced control, and machine learning.

STEVE DIXON is currently the Director of the Centre for Industrial Ultrasonics (CIU), University of Warwick, Coventry, U.K. He worked in the area of ultrasonics for 30 years and has published over 130 peer-reviewed journal articles. His research interests include ultrasonic measurements of material properties, non-contact ultrasound, non-destructive evaluation and testing, ultrasonic transduction, ultrasonic measurement of metallurgical microstructure, eddy current and electromagnetic inspection, and thermographic NDT. He held four research Fellowships, and is also a Co-Founding Member of the U.K. Research Centre for NDE (RCNDE).